V.V. USOV[1], N.M. SHKATULYAK[1], D.V. PAVLENKO[2], S.I. IOVCHEV[3], and D.V. TKACH[2,*]

[1] South Ukrainian National Pedagogical University
named after K.D. Ushinsky,
26 Staroportofrankivs'ka Str., UA-65020 Odesa, Ukraine

[2] Zaporizhzhia Polytechnic National University,
64 Zhukovs'ky Str., UA-69063 Zaporizhzhia, Ukraine

[3] Odesa National Maritime University,
34 Mechnikov Str., UA-65029 Odesa, Ukraine

* darynka.odarkivna@gmail.com

THE ELASTIC ANISOTROPY OF INCONEL 625 ALLOY SAMPLES MADE WITH 3*D* PRINTING

Depending on the 3*D*-printing orientation, the anisotropy of the elastic characteristics of the Inconel 625 alloy generated with selective laser sintering from powders is investigated. The impact of the original powder combination and the following heat treatment (post-printing treatment) on the anisotropy of the alloy elastic characteristics is assessed. As demonstrated, the suggested treatments can lessen the anisotropy of the alloy elastic characteristics. Based on knowledge of the elastic constants of the single crystal and x-ray texture features, the results of a theoretical estimation of the elastic and shear moduli, Poisson's ratio, and their anisotropy in the horizontal and vertical directions of 3*D* printing are provided. As demonstrated, the obtained theoretical values differ by 6–10% from the corresponding experimental values. The calculated stress–strain state can be more accurately calculated with the use of the estimated elastic characteristics and their anisotropy. The strategy for 3*D*-printing complicated components from Inconel 625 alloy may be made more effective.

Keywords: Inconel 625 alloy, additive manufacturing, selective laser sintering, crystallographic texture, mechanical properties, elastic anisotropy.

1. Introduction

New promising materials and methods for the manufacture of gas turbine engines have been studied and put into practice more and more recently [1]. It is well established that the utilization of diverse technological methods for powder consolidation, including hot isostatic pressing, hot rolling, friction stir processing [2, 3], selective laser melting [4] or severe plastic deformation [5], induces consequential alterations in both the structure and properties of the material.

The technique for creating complex-profile components *via* 3D printing includes the ability to generate individual parts elements in diverse directions. Understanding the mechanical behaviour of components is crucial in designing intricate technical systems like gas turbine engines. This assessment hinges on both the external load magnitude and the materials' physical and mechanical properties. In particular, the aerodynamic-surfaces' multidirectional spatial orientation exemplified by axial and centrifugal rotor wheels in compressor rotors and gas turbine engine turbines (Fig. 1) introduces a notable challenge. Assuming independence of the materials' elastic modulus from the direction leads to a considerable error in estimating the actual load levels.

Within the realm of heat-resistant alloys utilized in the fabrication of hot components for gas-turbine engines, Inconel 625 stands out as a quintessential representative. Due to its characteristics, it is well known that it is actively utilized in the petrochemical sector, essential in the construction of nuclear reactors, aeroplanes, gas turbines, and working blades for rocket and aviation engines. Spaceship parts have complicated geometries as well [7]. Selective laser sintering or melting techniques, sometimes known as 3D printing, are being employed more frequently for their manufacture in contemporary manufacturing [8].

To evaluate the strength of the produced products, it is crucial to choose the elastic parameters [9]. With additive manufacturing, metallic materials frequently acquire a crystallographic texture [10, 11]. As a result, elastic parameters become macroscopically anisotropic. To take advantage of anisotropy in the design process, proper prediction methods and experimental measurement of elastic parameters are needed to un-
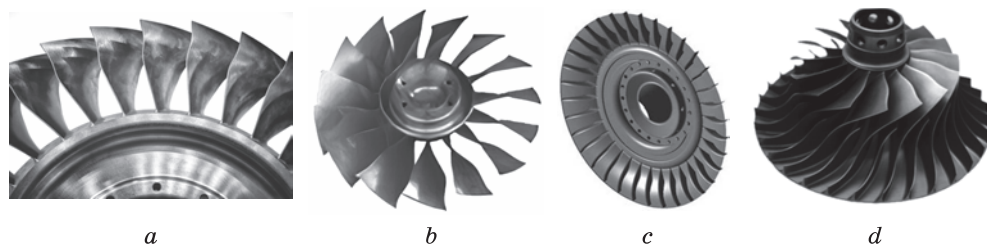

a	*b*	*c*	*d*

Fig. 1. Typical designs of modern monocycles (*a* and *b* — axial; *c* and *d* — centrifugal) [6]

derstand how processing factors affect the resultant texture. Given that the elastic modulus of a material is a property that directly influences accuracy, when identifying the stressed state of components, averaging its value for all elements of a part can result in known inaccuracies in computing its safety factor.

The study aims to analyse the elastic and shear moduli, Poisson's ratio, and their anisotropy determined from single-crystal elastic cons-tants and texture characteristics found by the x-ray diffraction in Inconel 625 alloy samples produced by selective powder technology in the horizontal and vertical directions of construction and then heated (post-treatment).

2. Materials and Methods

The samples were made by selective laser sintering of Inconel 625 (Al $\leq 0.4\%$; Co $\leq 1\%$; Cu $\leq 0.5\%$; Mn $\leq 0.5\%$; N $\leq 0.02\%$; S $\leq 0.015\%$; Si $\leq 0.5\%$; Ti $\leq 0.4\%$; C $\leq 0.1\%$; Cr 20−23%; Fe $\leq 5\%$; Mo 8−10%; Nb + Ta 3.15−4.15%; O $\leq 0.03\%$; P $\leq 0.015\%$; Ni — base), a nickel-based heat-resistant alloy powder. This alloy is designed to be used in the production of heavily loaded hot sections of gas turbine engines that operate at up to 700 °C.

Prismatic samples generated on an EOS M400 laser metal direct sintering installation served as the basis for establishing the patterns of crystallographic texture formation. Round granules served as the first component (powders). The first powder-mixture properties are listed in Ref. [12]. To obtain powders, the PREP (plasma rotating electrode process) technology was used.

Post-printing processing included hot isostatic pressing (HIP) to reduce voids and increase the density of the samples after 3D printing. In addition, the samples were subjected to heat treatment, which included holding the samples for 16 h at 900 °C (ageing). Details after printing can be found in Ref. [13].

Studies were performed on the samples that had been printed in various orientations both in their initial form (just after printing) and after further processing. The centre axis of the samples was parallel to the installation table in the horizontal direction (in the XY plane, toward the X-axis), and perpendicular to the installation table in the vertical direction (in the YZ plane in the direction of the Z-axis) (Fig. 2).

After 3D printing and post-processing, the samples' texture was examined using x-ray analysis. Figure 3 depicts the shooting plan.

To remove the flawed surface layer before the investigation, the samples were chemically polished to a depth of 0.1 mm. Using a DRON-3M general-purpose x-ray diffractometer and filtered MoK_α radiation, the θ−2θ scanning was performed. Inverse pole figures (IPFs) were created for various directions of the samples based on the survey data.

The polar density P_i is proportional to the ratio of the intensity of its diffraction line in the textured sample I_i to the intensity of the cor-
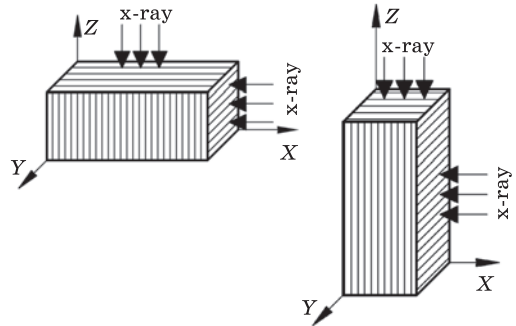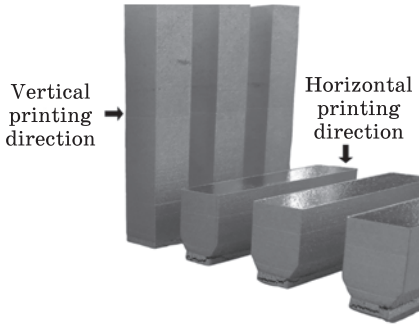
Fig. 2. Scheme of 3D printing of samples from Inconel 625 alloy

Fig. 3. Schematic of the sample built in the *XY*-plane (*a*) and a sample built in the *Z*-direction (*b*) [14]

responding line I_R of the sample without texture:

$$P_i = K \frac{I_i}{I_R},\qquad(1)$$

where the normalizing factor K according to Morris [15] is determined by the formula

$$K = \frac{1}{\sum_\Delta A_i (I_i/I_R)},\qquad(2)$$

where $\Sigma_\Delta A_i = 1$. The values of the coefficients $\{A_i\}$ are given in the literature [16].

Thus, the pole density reads as

$$P_i = \frac{I_i}{\sum_\Delta A_i (I_i/I_R)}.\qquad(3)$$

3. Results and Discussion

Table 1 lists the manufacturing strategy and post-processing treatment for obtaining the examined samples and for extra processing (post-treatment).

Figure 4 shows the IPFs of the studied samples after 3D printing and the corresponding post-printing treatment. Imaging was performed in the *Z*-direction, which is perpendicular to the *XY*-plane, and in the *X*-direction, which is perpendicular to the *ZY*-plane, for samples, which were built in the *XY*-plane.

The volume percentage of crystals of the matching orientation is known to be related to the pole density on the IPF. Based on this, it was assumed that the elastic properties of the examined polycrystalline samples in a given direction are the total of the particular contributions of the characteristics of single crystals of the appropriate orientation. The normalized value of the pole density on the IPFs of the corresponding direc-
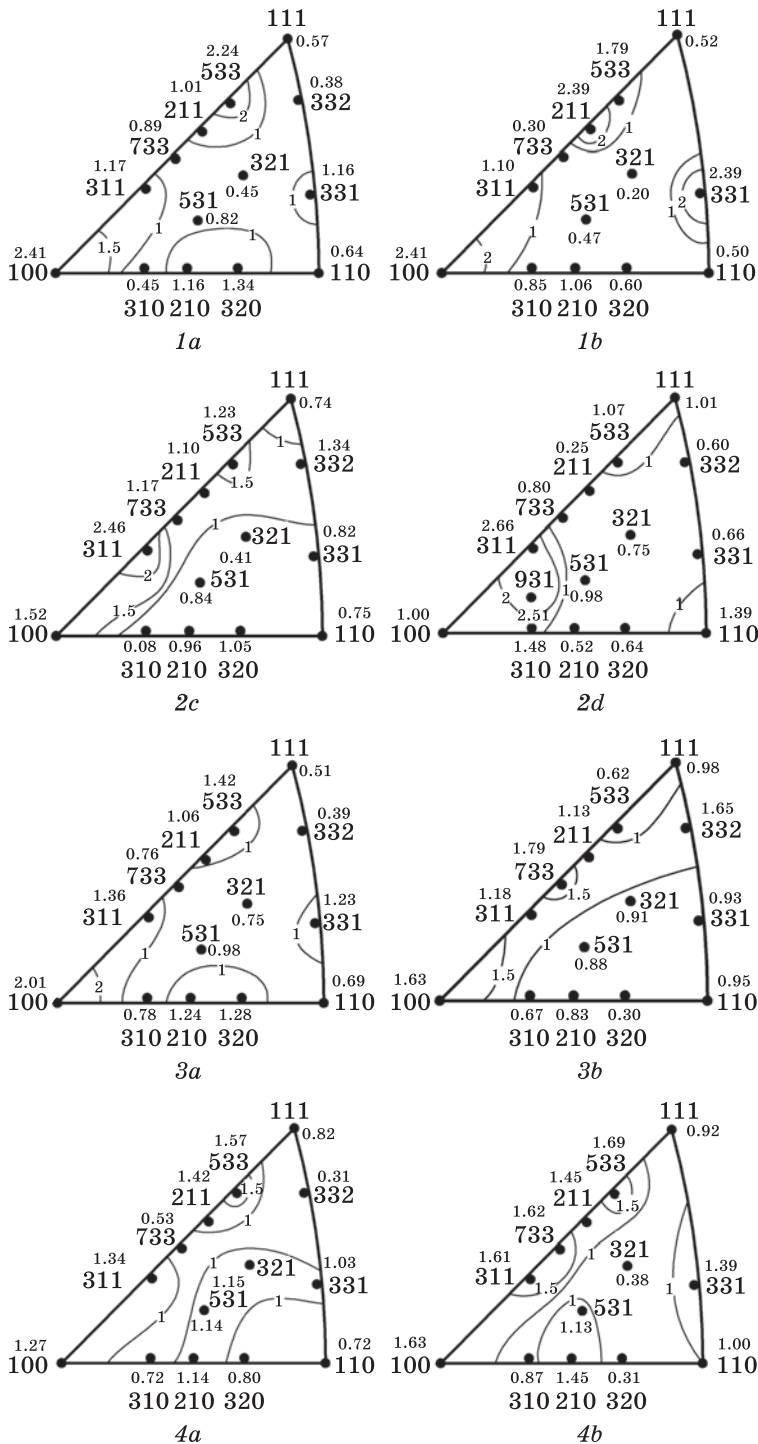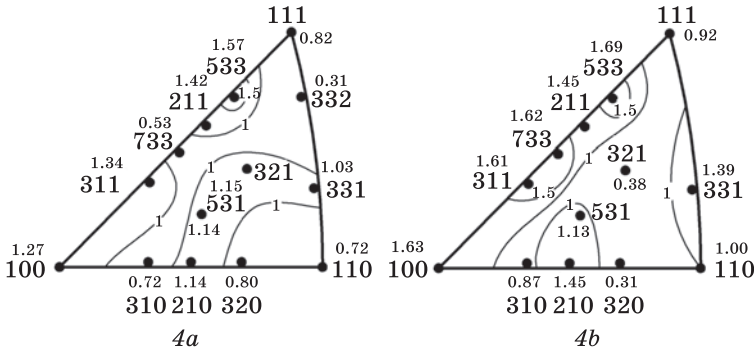
Fig. 4. Inverse pole figures of Inconel 625 alloy samples. The numbering of the IPF corresponds to the Table 1. IPFs with the letters *a* and *b* refer to samples built in the *XY*-plane, and IPFs with the letters *c* and *d* refer to samples built in the *Z*-direction

604

ISSN 1608-1021. Prog. Phys. Met., 2024, Vol. 25, No. 3

4a   *4b*

The End *Fig. 4*

Table 1. **Methods of manufacturing and post-processing the samples under consideration**

Sample No.	Direction of sample construction	Additional processing (post-treatment)
1	horizontal	without processing
2	verticalx	without processing
3	horizontal	quenching from 1190 °C + aging at 900 °C
4	horizontal	hot isostatic pressing and heat treatment
5	vertical	hot isostatic pressing and heat treatment

tion of the sample P_{hkl}^{N} determines the particular contribution, that is, the ratio of the pole density P_{hkl} to the total $\Sigma_{hkl} P_{hkl}$ of all those determined on the corresponding IPF:

$$P_{hkl}^{N} = \frac{P_{hkl}}{\sum_{hkl} P_{hkl}}. \tag{4}$$

Young modulus, shear, and Poisson's ratio of the studied samples were calculated using Miller indices $\langle hkl \rangle$ and the elastic compliances and moduli of the single crystal of the investigated alloy [17−19].

The inverse value of the modulus of elasticity of a single crystal is expressed through the Miller indices $\langle hkl \rangle$ by the well-known relationship [17, 18]:

$$\frac{1}{E_{hkl}} = S_{11} - 2S_0 \left[\frac{(hk^2) + (hl^2) + (lk^2)}{(h^2 + k^2 + l^2)} \right]. \tag{5}$$

The inverse shear modulus of a single crystal is related to the $\langle hkl \rangle$ direction by the following formula [19]:

$$\frac{1}{G_{hkl}} = S_{44} + 4S_0 \left[\frac{(hk^2) + (hl^2) + (lk^2)}{(h^2 + k^2 + l^2)} \right]. \tag{6}$$

The Poisson's ratio of a single crystal in the $\langle hkl \rangle$ direction can be determined by the formula [20]

$$\nu_{hkl} = \frac{1}{2} - \frac{E_{hkl}}{2(C_{11} + 2C_{12})}. \tag{7}$$

In the relations (5)–(7), S_{ij} and C_{ij} are elastic compliances and elastic moduli of a single crystal, respectively; $S_0 = S_{11} - S_{12} - S_{44}/2$; hkl are the Miller indices of the corresponding poles on the IPF.

To calculate the elastic characteristics of a polycrystal, it is necessary to take into account the normalized contributions of single crystals of certain orientations according to the ratio (4). Then, we have the relation for the corresponding properties of the polycrystal:

$$F_{\text{poly}}^{-1} = F_{hkl}^{-1} P_{hkl}^{N}, \tag{8}$$

where F is the corresponding property of a polycrystal (E, G or ν).

Table 2 displays the numerical values of elastic moduli C_{ij} from different sources.
Further computations were made using the averaged results because the numbers differ significantly. The following are the average elastic compliance values of an Inconel 625 single crystal, derived using established relationships [20] and the information in Table 2:

Table 2. **Elastic moduli of a single crystal of the Inconel 625 alloy (in [GPa])**

No.	C_{11}	C_{12}	C_{44}	$C_0 = C_{11} - C_{12} - 2C_{44}$	Ref.
1	243.0	152.0	117.8	−144.6	[21]
2	233.9	168.0	122.0	−179.0	[22]
3	243.3	156.7	117.9	−148.6	[23]
Average values	240.0	159.0	119.0	−157.0	

Table 3. **Calculated values of elastic properties of Inconel 625 alloy samples**

No. of the sample	Young modulus GPa				Shear modulus, GPa				Poisson's ratio			
	Construction direction				Construction direction				Construction direction			
	XY		Z		XY		Z		XY		Z	
	Calculation direction				Calculation direction				Calculation direction			
	Z	X	Z	X	Z	X	Z	X	Z	X	Z	X
1	206.0	206.0	—	—	75.1	68.5	—	—	0.315	0.326	—	—
2	—	—	203.0	205.0	—	—	69.1	69.8	—	—	0.323	0.317
3	198.6	196.1	—	—	68.4	68.4	—	—	0.314	0.314	—	—
4	205.0	202.0	—	—	67.8	67.5	—	—	0.320	0.317	—	—
5	—	—	204.0	201.0	—	—	68.5	68.3	—	—	0.319	0.317

$$S_{11} = 0.008092321 \ (8.827 \cdot 10^{-12} \ \text{Pa}^{-1});$$

$$S_{12} = -0.003143634 \ (-3.518 \cdot 10^{-12} \ \text{Pa}^{-1});$$

$$S_{44} = 0.009009009 \ (8.403 \cdot 10^{-12} \ \text{Pa}^{-1});$$

$$S_0 = S_{11} - S_{12} - 0.5 \times S_{44} = 0.006731451 \ (8.1443 \cdot 10^{-12} \ \text{Pa}^{-1}).$$

The normalized values of the pole density on the IPF were calculated using relation (3).

Table 3 shows the calculation results of elastic modulus, shear modulus, and Poisson's ratio using Eqs. (5)–(8). As seen from Table 3, the characteristics under study are anisotropic. So for samples after 3D printing without additional processing (Nos. 1 and 2), the elastic properties calculated in the same directions (Nos. 1X, 2X and Nos. 1Z, 2Z) are different. The differences were 0.5–1.5%, 1.9–8.7%, and 0.9–2.5%, for E, G, and ν, respectively. The elastic properties of sample No. 1 calculated in the X-direction and sample No. 2 calculated in the Z-direction (*i.e.*, No. 1X and No. 2Z) are also different. The differences were by ≈1.5% for Young modulus, ≈7.6% for shear modulus, and ≈0.9% for Poisson's ratio. In this case, Young moduli of horizontal samples exceed the values of the corresponding properties of vertical samples. Comparative trends are indicated in Refs. [12, 24–26].

In the work [26] for the sample constructed in the Z-direction, the value E = 196 GPa is given. We obtained for a vertical sample (No. 2Z) the value E = 203 GPa (a difference of 3.6%). It is shown from Ref. [24] that, with an increase in the volumetric energy density during 3D printing from ≈80 to 155 J/mm³, Young modulus of horizontal samples of the Inconel 625 alloy can vary from ≈140 to 205 GPa, and for vertical samples from ≈90 to 175 GPa.

In Ref. [23], the experimental value E = 152 GPa is given, which differs significantly from the values in our work. It should be noted that the value of Young modulus was obtained in Ref. [23] during compression tests using electron diffraction, in contrast to the experimental data in Ref. [24] obtained during classical tensile tests. It is not also reported in Ref. [23], whether this value corresponds to the horizontal or vertical direction of the sample building. Estimating the volumetric energy density during sample fabrication in Ref. [23] is also difficult.

When comparing our calculated values of the elastic moduli in the X direction of the horizontal sample and the Z direction of the vertical sample (samples Nos. 1 and 2) with the corresponding experimental values obtained in Ref. [25], it turned out that the deviation is approximately from 4 to 9%. For the shear modulus of samples after 3D printing, values of 75 GPa and 65 GPa are given in Ref. [25] for samples printed in the XY-plane and Z-direction, respectively. Comparison with those we
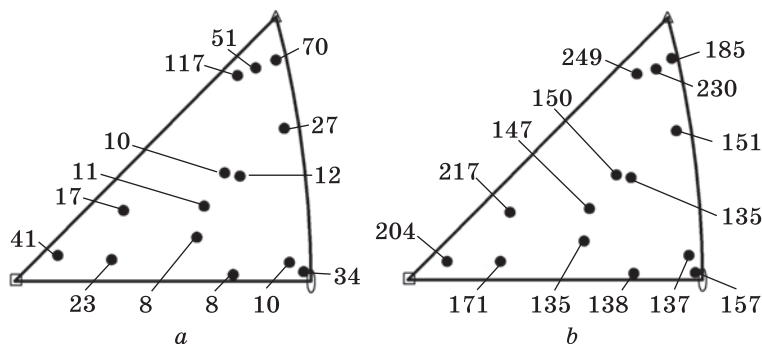
Fig. 5. Hardening coefficients (MPa) of copper crystals of 99.88% purity at the first (a) and second (b) stages of hardening for different orientations [28]

obtained in Table 3 for samples 1 and 2 after printing showed a deviation within 6–7%. The Poisson's ratio of the samples after 3*D* printing in Ref. [25] varies from 0.45 (in the *XY* plane) to 0.27 in the *Z*-direction. The values of Poisson's ratio we calculated do not exceed the limits specified in Ref. [25].

Table 3 shows that subsequent quenching after 3*D* printing from 1190 °C with ageing at 900 °C (sample No. 3) contributes to a slight decrease in the elastic modulus and a corresponding increase in the displacement modulus and Poisson's ratio. Additional heat treatment (HIP + HT) after 3*D* printing (samples Nos. 4 and 5) contributes to a slight increase in the elastic modulus of the Inconel 625 alloy (also observed in Ref. [27]) in contrast to the Inconel 718 alloy, in which a similar thermal treatment after printing increases the moduli elasticity [11].

Analysis of experimental IPFs presented in Fig. 4 showed that on the IPFs the highest values of the pole density are located along the diagonal [001]–[111] of the stereographic triangle. The mechanisms of the formation of crystallographic texture in f.c.c. metals and alloys after various types of deformation and subsequent heat treatment are quite well known [28]. Moreover, crystallographic texture is one of the main reasons for the anisotropy of mechanical properties. An analysis of the deformation of metal crystals with an f.c.c. lattice showed [28] that the strengthening during deformation could vary over a wide range depending on the orientation of the crystals. Crystallites with orientations are located close to or on the boundary of the [001]–[111] side of the stereographic triangle, towards which the tensile axis approaches during deformation, show strengthening greater than crystallites whose orientations lie in the central region of the stereographic triangle. Crystallites whose orientations are especially far from the side of [001]–[111], turn out to be less durable when stretched. The greatest strengthening was found in crystals

with [001] and [111] orientations, both at the first and second stages of strengthening, although not as pronounced (Fig. 5) [28].

The formation of crystallographic texture in the 3*D*-printing process has been studied much less, as mentioned above. The formation of the ⟨100⟩-texture component is probably because columnar crystals grow fastest, in which the orientation forms a minimal angle with the direction of maximal heat removal. In f.c.c. alloys (which also includes Inconel 625), the orientations [111] deviated from the [001] crystallographic direction by 54°. As a result, after selective laser sintering during the 3*D* printing, any neighbouring grains of other orientations [29] can suppress the crystallization of grains with orientations [111]. It is likely for these reasons that the pole density ⟨111⟩ on the IPFs is low, while the pole densities ⟨533⟩ and ⟨100⟩ are relatively high (Fig. 3).

As is known, the pole density on the IPF (Fig. 4) is proportional to the volume fraction of crystals of the corresponding orientation. Based on the above, to predict the influence of crystal orientation on the strength properties of samples of the alloy under study, one can use the value of the total pole density of crystal orientations along the [001]–[111] $\Sigma_{[001]-[111]}P_{hkl}$ for the stereographic triangle side samples in the horizontal and vertical construction directions. Analysis of the total pole density obtained on the IPF in the *X*-direction of samples built in the plane *XY* and on the IPF taken in the *Z*-direction of samples constructed in the *Z*-direction (Nos. 1*b*, 2*c*, 4*b*, and 5*c*) showed that, after 3*D* printing, the total pole density of horizontal samples exceeds the corresponding value of vertical ones. So, the total pole density of sample No. 1*b* $\Sigma_{[001]-[111]}P_{hkl} = 8.51$, and for sample No. 2*c*, $\Sigma_{[001]-[111]}P_{hkl} = 8.22$; similarly, for sample No. 4*b*, $\Sigma_{[001]-[111]}P_{hkl} = 8.50$, and for sample No. 5*c*, $\Sigma_{[001]-[111]}P_{hkl} = 8.11$. We can expect that, as a result, the strength properties of horizontal samples may be higher, and, accor-

Table 4. **Mechanical properties of Inconel 625 alloy samples after 3*D* printing and subsequent heat treatment. Here, AB denotes the sample in the state 'Initial, as built', whereas HT denotes the sample in the state 'after heat treatment'**

| No. | Ultimate tensile strength (UTS), MPa | | | | Yield strength (YS), MPa | | | | Elongation d, % | | | | Ref. |
| | XY | | Z | | XY | | Z | | XY | | Z | | |
	AB	HT	AB	HT	AB	HT	AB	HT	AB	HT	AB	HT	
1	990	—	900	—	725	—	615	—	35	—	42	—	[24]
2	780	—	705	—	530	—	450	—	11.8	—	11.2	—	[25]
3	1250	1140	1121	1030	915	695	845	615	40.0	47.7	41.0	52.5	[30]
	1300	1192	1100	1012	928	719	825	650	41.2	46.7	41.7	51.0	
4	910	—	840	—	390	—	380	—	62	—	55	—	[31]
5	—	882	—	869	—	438.5	—	433.5	—	56.4	—	59.0	[13]
		881		866		448.0		433.0		48.4		57.3	

dingly, the plastic characteristics of the horizontally constructed samples are lower than those for the vertical ones are.

An analysis of the literature on the mechanical properties of Inconel 625 alloy samples produced by 3D printing and subjected to further heat treatment showed that the above was correct (Table 4). This suggests that the crystallographic texture is the main reason for the anisotropy of the characteristics of the studied samples of the Inconel 625 alloy. Consequently, rational use of the crystallographic texture, provided by selective laser sintering in the corresponding directions of the sample, can be manufactured parts with an optimal set of qualities.

4. Conclusions

The crystallographic texture studied of Inconel 625 alloy samples obtained from powders by 3D printing in the horizontal and vertical directions and after heat treatment. It was found that the total pole density on the [001]–[111] diagonal of a spherical triangle on the inverse pole figures of horizontal samples exceeds the value of the corresponding total pole density on the [001]–[111] diagonal of a spherical triangle on the IPF of vertical ones. This can be used for predictive assessment of mechanical properties, as shown by a comparative analysis of the IPF pole density and the corresponding mechanical properties from literature sources of samples of the studied alloy.

Using the elastic constants of alloy single crystal and pole density data on the IPF, the elastic moduli, shear modulus, Poisson's ratio, and their anisotropy of alloy samples of the Inconel 625 alloy after 3D printing from powders in the horizontal and vertical construction directions and after post-printing heat treatment were evaluated.

The elastic moduli of the horizontal samples determined in the X-direction are higher than the vertical sample elastic moduli determined in the Z-direction. The shear modulus and Poisson's ratio showed the opposite trend.

The calculated values of the elastic modulus deviate from the experimental data by $4-6\%$. For the shear modulus, the corresponding difference was $6-7\%$. The calculated values of Poisson's ratio of the Inconel 625 alloy after 3D printing and post-printing processing $(0.312-0.342)$ do not exceed the limits of $0.45-0.27$ specified in Ref. [25].

Subsequent quenching after 3D printing from 1190 °C with ageing at 900 °C (sample No. 3) contributes to a slight decrease in the elastic modulus and a corresponding increase in the displacement modulus and Poisson's ratio.

Additional heat treatment (HIP + HT) after 3D printing (samples Nos. 4 and 5) contributes to a slight increase in the elastic modulus of the Inconel 625 alloy.

REFERENCES

1. D. Pavlenko, Y. Dvirnyk, and R. Przysowa, *Aerospace*, **8**, No. 1: 1 (2021).
   https://doi.org/10.3390/aerospace8010001
2. S. Yin, N. Fan, C. Huang, Y. Xie, C. Zhang, R. Lupoi, and W. Li, *J. Mater. Sci. Technol.*, **170**: 47 (2024);
   https://doi.org/10.1016/j.jmst.2023.05.047
3. V.G. Mishchenko and S.P. Sheyko, *Steel Transl.*, **44**, No. 12: 928 (2014);
   https://doi.org/10.3103/s0967091214120122
4. J.-U. Lee, Y.-K. Kim, S.-M. Seo, and K.-A. Lee, *Mater. Sci. Eng. A*, **841**: 143083 (2022);
   https://doi.org/10.1016/j.msea.2022.143083
5. D. Pavlenko and A. Ovchinnikov, *Mater. Sci.*, **51**, No. 1: 52 (2015);
   https://doi.org/10.1007/s11003-015-9809-9
6. V.A. Boguslaev, V.K. Yatsenko, P.D. Zhemanyuk, G.V. Pukhalskaya, D.V. Pavlenko, and V.P. Ben, *Otdelochno-Uprochnyayushchaya Obrabotka Detaley GTD* [Finishing-Strengthening Treatment of Gas Turbine Engine Parts] (Zaporozh'ye: OAO 'Motor Sich': 2005) (in Russian).
7. M. Jimenez, L. Romero, I.A. Dominguez, M. Espinosa, and M. Dominguez, *Complexity*, **2019**: 9656938 (2019);
   https://doi.org/10.1155/2019/9656938
8. B. Zhang, Y. Li, and Q. Bai, *Chin. J. Mech. Eng.*, **30**, No. 3: 515 (2017);
   https://doi.org/10.1007/s10033-017-0121-5
9. A.M. Polyanskiy, V.A. Polyanskiy, A.K. Belyaev, and Y.A. Yakovlev, *Acta Mech.*, **229**: 4863 (2018);
   https://doi.org/10.1007/s00707-018-2262-8
10. T. Obermayer, C. Krempaszky, and E. Werner, *Metals*, **12**, No. 11: 1991 (2022);
    https://doi.org/10.3390/met12111991
11. V.V. Usov, N.M. Shkatuliak, N.I. Rybak, M.O. Tsarenko, D.V. Pavlenko, D.V. Tkach, and O.O. Pedash, *Metallofiz. Noveishie Tekhnol.*, **45**, No. 1: 111 (2023);
    https://doi.org/10.15407/mfint.45.01.0111
12. H.L. Eiselstein and D.J. Tillack, *The Invention and Definition of Alloy 625*, *Superalloys 718, 625 and Various Derivatives* (Warrendale, Pennsylvania: 1991), p. 1;
    https://doi.org/10.7449/1991/Superalloys_1991_1_14
13. N.O. Lysenko, O.O. Pedash, V.V. Klochykhin, and P.O. Kasai, *Electrometallurgy Today*, **4**: 38 (2021);
    https://doi.org/10.37434/sem2021.04.06
14. V.V. Usov, N.M. Shkatuliak, D.V. Pavlenko, and O.M. Tkachuk, *Mater. Sci.*, **59**: 414 (2023);
    https://doi.org/10.1007/s11003-024-00792-9
15. P.R. Morris, *J. Appl. Phys.*, **30**, No. 5: 595 (1959);
    https://aip.scitation.org/doi/10.1063/1.1702413
16. Ya.D. Vishnyakov, *Teoriya Obrazovaniya Tekstur v Metallakh i Splavakh* [The Theory of Texture Formation in Metals and Alloys] (Moskva: Nauka: 1979) (in Russian).
17. P. Aba-Perea, T. Pirling, P. Withers, J. Kelleher, S. Kabra, and M. Preuss, *Mater. Des.*, **89**, No. 5: 856 (2016);
    https://doi.org/10.1016/j.matdes.2015.09.152
18. J. Everaerts, C. Papadaki, W. Li, and A.M. Korsunsky, *J. Mech. Phys. Solids*, **131**: 303 (2019);
    https://doi.org/10.1016/j.jmps.2019.07.011

19. L. Zhang, R. Barrett, P. Cloetens, C. Detlefs, and M. Sanchez del Rio, *J. Synchrotron Radiat.*, **21**, No. 3: 507 (2014);
https://doi.org/10.1107/S1600577514004962

20. J.F. Nye, *Physical Properties of Crystals: Their Representation by Tensors and Matrices* (Oxford: Clarendon Press: 1985).

21. J. Rossin, P. Leser, J.T. Benzing, C. Torbet, R.P. Dillon, S. Smith, S. Daly, and T.M. Pollock, *NDT & E Int.*, **135**: 102803 (2023);
https://doi.org/10.1016/j.ndteint.2023.102803

22. J.M. Ortiz-Roldan, *Phys. Chem. Chem. Phys.*, **20**: 18647 (2018);
https://www.rsc.org/suppdata/c8/cp/c8cp02591f/c8cp02591f1.pdf

23. Z. Wang, A.D. Stoica, D. Ma, and A.M. Beese, *Mater. Sci. Eng. A*, **674**: 406 (2016);
https://doi.org/10.1016/j.msea.2016.08.010

24. S.P. Kumar, S. Elangovan, R. Mohanraj, and J.R. Ramakrishna, *Mater. Today: Proc.*, **46**, No. 17: 7892 (2021);
https://doi.org/10.1016/j.matpr.2021.02.566

25. H.R. Javidrad and S. Salemi, *Int. J. Adv. Manuf. Technol.*, **107**: 4597 (2020);
https://doi.org/10.1007/s00170-020-05321-x

26. *Ni-Alloy IN625 / 2.4856 / B446. Material Data Sheet*;
https://www.slm-solutions.com/fileadmin/Content/Powder/MDS/MDS_Ni-Alloy_IN625_0819_EN.pdf

27. G. Marchese, M. Lorusso, S. Parizia, E. Bassini, J.-W. Lee, F. Calignano, D. Manfredi, M. Terner, H.-U. Hong, D. Ugues, M. Lombardi, and S. Biamino, *Mater. Sci. Eng. A*, **729**: 64 (2018);
https://doi.org/10.1016/j.msea.2018.05.044

28. R.V.K. Honeycombe, *The Plastic Deformation of Metals* (London: Edward Arnold Ltd. Publ.: 1984);
https://archive.org/details/plasticdeformati0000hone_c4v2/page/n5/mode/2up?view=theater

29. J. Zhu, C. Shao, F. Lu, K. Feng, P. Liu, S. Chu, Y. Feng, H. Kokawa, and Z. Li, *Scr. Mater.*, **221**: 114945 (2022);
https://doi.org/10.1016/j.scriptamat.2022.114945

30. Md.A. Anam, *Microstructure and Mechanical Properties of Selective Laser Melted Superalloy Inconel 625*, Electronic Theses and Dissertations (2018), Paper 3029;
https://doi.org/10.18297/etd/3029

31. J.A. Gonzalez, J. Mireles, S.W. Stafford, M.A. Perez, C.A. Terrazas, and R.B. Wicker, *J. Mater. Process. Technol.*, **264**: 200 (2019);
https://doi.org/10.1016/j.jmatprotec.2018.08.031

В.В. Усов[1], *Н.М. Шкатуляк*[1], *Д.В. Павленко*[2], *С.І. Іовчев*[3], *Д.В. Ткач*[2]

[1] Південноукраїнський національний педагогічний університет ім. К.Д. Ушинського,
вул. Старопортофранківська, 26, 65020 Одеса, Україна

[2] Національний університет «Запорізька політехніка»,
вул. Жуковського, 64, 69063 Запоріжжя, Україна

[3] Одеський національний морський університет,
вул. Мечникова, 34, 65029 Одеса, Україна

ПРУЖНА АНІЗОТРОПІЯ ЗРАЗКІВ СПЛАВУ INCONEL 625, ВИГОТОВЛЕНИХ 3D-ДРУКОМ

Залежно від орієнтації 3D-друку досліджено анізотропію пружних характеристик сплаву Inconel 625, одержаного методом селективного лазерного спікання з порошків. Оцінено вплив вихідної комбінації порошків і подальшого термічного оброблення (після друку) на анізотропію пружних характеристик сплаву. Показано, що пропоновані способи оброблення можуть зменшити анізотропію пружних характеристик сплаву. На основі знання пружних констант монокристала й особливостей рентгенівської текстури наведено результати теоретичного оцінювання модулів пружності та зсуву, пуассонова коефіцієнта й їхньої анізотропії в горизонтальному та вертикальному напрямках 3D-друку. Показано, що одержані теоретичні значення відрізняються на 6–10% від відповідних експериментальних значень. За допомогою оцінених пружних характеристик та їхньої анізотропії можна більш точно розрахувати напружено-деформований стан, а також зробити ефективнішою стратегію 3D-друку складних деталей зі сплаву Inconel 625.

Ключові слова: сплав Inconel 625, адитивне виробництво, селективне лазерне спікання, кристалографічна текстура, механічні властивості, пружна анізотропія.